

Electron acceleration due to high frequency instabilities at supernova remnant shocks

M. E. Dieckmann,^{a,1} K. G. McClements,^{b,2} S. C. Chapman,^a
R. O. Dendy,^{b,a} and L. O’C. Drury^c

^a Space and Astrophysics Group, Department of Physics, University of Warwick,
Coventry, CV4 7AL, UK

^b EURATOM/UKAEA Fusion Association, Culham Science Centre, Abingdon,
Oxfordshire OX14 3DB, UK

^c Dublin Institute for Advanced Studies, 5 Merrion Square, Dublin 2, Ireland

To appear in *Astronomy and Astrophysics* (accepted: February 15 2000)

Abstract

Observations of synchrotron radiation across a wide range of wavelengths provide clear evidence that electrons are accelerated to relativistic energies in supernova remnants (SNRs). However, a viable mechanism for the pre-acceleration of such electrons to mildly relativistic energies has not yet been established. In this paper an electromagnetic particle-in-cell (PIC) code is used to simulate acceleration of electrons from background energies to tens of keV at perpendicular collisionless shocks associated with SNRs. Free energy for electron energization is provided by ions reflected from the shock front, with speeds greater than the upstream electron thermal speed. The PIC simulation results contain several new features, including: the acceleration, rather than heating, of electrons via the Buneman instability; the acceleration of electrons to speeds exceeding those of the shock-reflected ions producing the instability; and strong acceleration of electrons perpendicular to the magnetic field. Electron energization takes place through a variety of resonant and non-resonant processes, of which the strongest involves stochastic wave-particle interactions. In SNRs the diffusive shock process could then supply the final step required for the production of fully relativistic electrons. The mechanisms identified in this paper thus provide a possible solution to the electron pre-acceleration problem.

¹Present address: Institutet för teknik och naturvetenskap, Linköpings Universitet, Campus Norrköping, S-601 74 Norrköping, Sweden

²Corresponding author. E-mail: k.g.mcclements@ukaea.org.co.uk

1 Introduction

The detection of radio synchrotron emission from shell-type supernova remnants (SNRs) is a clear indication that electrons of typically GeV energy are being accelerated in such objects. There is now convincing evidence that synchrotron emission from some remnants extends to X-ray wavelengths (Pohl & Esposito 1998): this implies the presence of electrons with energies of order 10^{14} eV. The prime example of this is the remnant of SN1006, recent observations of which using the ASCA (Koyama et al. 1995) and ROSAT (Willingale et al. 1996) spacecraft show that X-ray emission from the bright rim has a hard, approximately power-law spectrum. In contrast, emission from the centre is softer, with a strong atomic line component. The sharp edges and strong limb brightening observed at both X-ray and radio wavelengths indicate that: the acceleration site is the strong outer shock bounding the remnant; the acceleration is continuous; and the local diffusion coefficient of electrons near the shock front is substantially reduced relative to that in the general interstellar medium (Achterberg et al. 1994). The possibility that the X-ray emission from SN1006 is thermal bremsstrahlung has been examined by Laming (1998), and found to be less tenable than the synchrotron interpretation.

There is thus extensive observational evidence that the strong collisionless shocks bounding shell-type SNRs accelerate electrons to relativistic energies. The standard interpretation of extragalactic radio jet observations is also based on the premise that the relativistic electrons responsible for observed synchrotron emission are produced by shocks, although in this case the shock parameters are much less certain. Heliospheric shocks, on the other hand, do not generally appear to be associated with strong electron acceleration, perhaps because the Mach numbers of such shocks are much lower than those of SNRs and extragalactic radio jets, although Anderson et al. (1979) have published data showing that keV electrons are produced in the vicinity of the perpendicular bow shock of the Earth.

While diffusive shock acceleration (Axford et al. 1977; Krymsky 1977; Bell 1978; Blandford & Ostriker 1978) provides an efficient means of generating highly energetic electrons from an already mildly relativistic threshold, and can operate at oblique shocks as well as parallel ones (Kirk & Heavens 1989), the “injection” or “pre-acceleration” question remains very open: by what mechanisms can electrons be accelerated from background (sub-relativistic) energies to mildly relativistic energies (Levinson 1996)? In this

paper, we investigate one of the possible answers, which has attractive “bootstrap” characteristics. Specifically, we suggest that waves are excited by collective instability of the non-Maxwellian population of ions reflected from a perpendicular shock front, and that these waves damp on thermal electrons, thereby accelerating them. Such a process was first proposed as a candidate acceleration mechanism for cosmic ray electrons by Galeev (1984). This model was developed further by Galeev et al. (1995), with the added ingredient of macroscopic electric fields implied by the need to maintain quasi-neutrality in a plasma with an escaping population of electrons. McClements et al. (1997) carried out a primarily analytical study of electron acceleration by ion-excited waves at quasi-perpendicular shocks, which was necessarily restricted to quantifying linear régimes of wave excitation and particle acceleration, in relation to inferred shock parameters.

Instabilities driven by shock-reflected ions at SNR shocks have also been invoked by Papadopoulos (1988) and Cargill & Papadopoulos (1988) as mechanisms for electron heating, rather than electron acceleration. On the basis of a simple analytical calculation, Papadopoulos predicted that strong electron heating would occur at quasi-perpendicular shocks with “superhigh” Mach numbers (specifically, shocks with fast magnetoacoustic Mach numbers $M_F > 30\text{--}40$) through the combined effects of Buneman (two-stream) and ion acoustic instabilities. In this model the Buneman instability, driven by the relative streaming of shock-reflected ions and upstream electrons, heats the electrons to a temperature T_e much greater than the ion temperature T_i : in these circumstances, the ion acoustic instability can be driven unstable if there is a supersonic streaming between the electrons and either reflected or non-reflected (“background”) ions. Using a hybrid code, in which ions were treated as particles and electrons as a massless fluid, Cargill & Papadopoulos (1988) found that the electron heating predicted by Papadopoulos (1988) could occur in a self-consistently computed shock structure. However, as Cargill & Papadopoulos point out in the last paragraph of their 1988 paper, the use of a fluid model for the electrons means that hybrid codes cannot be used to investigate electron acceleration. Recently, Bessho & Ohsawa (1999) have used a particle-in-cell (PIC) code to investigate acceleration of electrons from tens of keV to highly relativistic energies at oblique shocks in which the electron gyrofrequency Ω_e exceeds the electron plasma frequency ω_{pe} .

An improved theoretical understanding of electron acceleration at shocks is desirable not only for intrinsic interest, but also to enable observations

of synchrotron and inverse Compton emission to be related quantitatively to shock parameters. However, almost all work on particle acceleration has concentrated on ions. There are several reasons for this. First, upstream momentum and energy fluxes are dominated by ions, and the shock structure problem therefore reduces essentially to that of isotropizing the ion distribution. Second, much of our understanding is based on the use of hybrid codes, in which electrons are represented as a fluid: such codes cannot provide information on electron acceleration. However, the very fact that electron dynamics does not appear to be important for shock structure allows us to separate the two problems: prescribing the ion parameters using the results of hybrid code simulations, we can examine in detail physical processes occurring on electron timescales. This is the approach followed in this paper. We describe the results of a fully nonlinear investigation, carried out by large scale numerical simulation using a PIC code and backed up by analytical and numerical studies, of the underlying plasma physics mechanisms. We consider the case $\omega_{pe} > \Omega_e$, which is qualitatively distinct from the strongly-magnetized régime investigated by Bessho & Ohsawa (1999). Our primary goal is finding a mechanism capable of producing mildly relativistic electrons: once they have attained rigidities comparable to those of shock-heated protons, they can undergo resonant scattering, and subsequent acceleration to relativistic energies can then proceed via the diffusive shock mechanism. Our approach enables us to test earlier predictions of both electron acceleration (Galeev 1984; Galeev et al. 1995; McClements et al. 1997) and electron heating (Papadopoulos 1988; Papadoulos & Cargill 1988) at very high Mach number astrophysical shocks. Simulation results are presented for a range of reflected ion speeds in Sect. 2; plasma instabilities occurring in the simulations, and other processes likely to play a role in electron acceleration and heating at SNR shocks, are identified in Sect. 3; and the results of these investigations are discussed in Sect. 4.

2 Particle-in-cell code simulations

To investigate wave excitation and particle acceleration in the vicinity of a perpendicular SNR shock we use an electromagnetic relativistic PIC code described by Devine (1995). The particle-in-cell principle (Denavit & Kruer 1980) relies on self-consistent evolution of electromagnetic fields and macroparticles in sequential stages. Relativistic electromagnetic PIC codes have been

used previously to simulate acceleration processes in astrophysical plasmas (e.g. McClements et al. 1993; Bessho & Ohsawa 1999). A distinctive feature of the code used in the present study is the fact that the energy density of electromagnetic or electrostatic fluctuations can be readily determined as a function of frequency ω , wavevector k or time t : this greatly facilitates the identification of any wave modes excited in a particular simulation.

The code has one space dimension (x) and three velocity dimensions (v_x, v_y, v_z). To model a plasma containing shock-reflected proton beams, we construct a simulation box with 350 grid cells in the x -direction and with the local magnetic field \mathbf{B} oriented in the y -direction. McClements et al. (1997) pointed out that, at any given point in the shock foot, there are in fact two proton beams, one propagating away from the shock, the other towards it. For simplicity, we assume in our PIC model that the two beams propagate with equal speeds $u_{b\perp}$ in opposite directions perpendicular to the magnetic field, and that both background ions and electrons have zero net drift: thus, the simulated plasma has zero current. Strictly speaking, this is unrealistic, since, in self-consistent models of perpendicular shocks, the magnetic field magnitude has a finite gradient along the shock normal direction, and a finite current is then required by Ampère’s law (Woods 1969). We will discuss this approximation in Sect. 4. The frame of reference in each simulation is the upstream plasma frame: time evolution in the simulation can thus be interpreted as spatial variation in the shock foot, with $t = 0$ in the simulation corresponding to the interface between the undisturbed upstream plasma and the foot. The size of the foot L_{foot} lies approximately in the range $(0.3 - 0.7)v_s/\Omega_i$, where v_s is the shock speed and Ω_i is the upstream ion gyrofrequency (McClements et al. 1997). Thus, if the simulation is to be confined to the foot, the duration of the simulation should be no greater than

$$t_{\text{max}} = \frac{L_{\text{foot}}}{v_s} \simeq (88 - 205) \frac{2\pi}{\Omega_e}, \quad (1)$$

where Ω_e is the electron gyrofrequency (the true proton/electron mass ratio, 1836, was used in the simulations). The simulations reported here lasted for either 70 or 135 electron cyclotron periods $2\pi/\Omega_e$.

The proton beams were assumed to be initially Maxwellian with thermal speed $\delta u_{\perp} = 3 \times 10^5 \text{ ms}^{-1}$ (δu_{\perp} being defined such that the equivalent temperature in energy units is $m_p \delta u_{\perp}^2$, where m_p is the proton mass), and a range of perpendicular drift speeds $u_{b\perp} = 3.25v_{e0}, 3.5v_{e0}, 5v_{e0}$ and $6v_{e0}$, where v_{e0} is the electron thermal speed, defined in the same way as δu_{\perp} and

initially set equal to $3.75 \times 10^6 \text{ ms}^{-1}$ (this corresponds to an electron temperature $T_e \simeq 9.3 \times 10^5 \text{ K} \simeq 80 \text{ eV}$). The value chosen for the total beam number density, $0.33n_e$, is consistent with the highest values of this parameter found in hybrid simulations of quasi-perpendicular shocks with Alfvénic Mach numbers M_A ranging up to about 60 (Quest 1986). Cargill & Papadopoulos (1988) used $M_A = 50$ in their hybrid simulation of an SNR shock (it was computationally difficult to simulate shocks with higher M_A). The density of each beam n_b is, accordingly, one sixth of the electron density n_e , so that the background proton density n_i required by charge balance is $0.67n_e$ (the background proton thermal speed v_i was set equal to $1.9 \times 10^5 \text{ ms}^{-1}$). The electron plasma frequency $\omega_{pe}/2\pi$ and gyrofrequency $\Omega_e/2\pi$ in our simulations were set equal to 10^5 Hz and 10^4 Hz , respectively, corresponding to $n_e \simeq 1.2 \times 10^8 \text{ m}^{-3}$ and magnetic field $B \simeq 3.6 \times 10^{-7} \text{ T}$. The ratio ω_{pe}/Ω_e is typically of order 10^2 or higher in HII regions of the interstellar medium. We have chosen a relatively low value of this ratio in order to study and compare the effects of instabilities occurring on both the ω_{pe}^{-1} and Ω_e^{-1} timescales.

The electrons, background protons and each proton beam were represented, respectively, by 3200, 800 and 7200 particles per cell. The use of a relatively small number of background protons per cell is justified by the fact that instabilities driven by the proton beams have much higher frequencies than noise fluctuations associated with the background protons: large numbers of electrons and beam protons in each cell ensure a level of noise energy well below the wave energy produced by the instabilities. In what follows we measure time in electron cyclotron periods, using the notation $\tilde{t} = \Omega_e t / 2\pi$. We also define $\tilde{k} = kv_{e0}/\Omega_e$ (only waves propagating in the x -direction are represented), a normalized frequency $\tilde{\omega} = \omega/\Omega_e$, and $r = kv_{\perp}/\Omega_e$, v_{\perp} being electron velocity perpendicular to the magnetic field.

In every simulation, transfer of energy from beam protons to electrons was observed, but the power flux between the two species increased dramatically when $u_{b\perp}$ was raised from $3.5v_{e0}$ to $5v_{e0}$. Figure 1 is a time evolution plot of perpendicular kinetic energy $\mathcal{E}_{\perp e} = \sum_j m_e v_{\perp j}^2 / 2$, where m_e is electron mass and the summation is over all electrons in the simulation box. Since the total electron number is constant, $\mathcal{E}_{\perp e}$ can be regarded as a measure of the effective perpendicular electron temperature (although it should be stressed at the outset that the electrons do not always have a Maxwellian distribution). The energy is normalized to its initial value, which was identical in the four simulations. When $u_{b\perp} = 3.25v_{e0}$ and $3.5v_{e0}$ (upper plot) the energy increases by approximately an order of magnitude in around 60–100 electron cyclotron

periods; when $u_{b\perp} = 5v_{e0}$ and $6v_{e0}$ (lower plot) the energy increases by a factor of about 40 within $\tilde{t} \simeq 15-30$. The perpendicular energies of the other two particle populations, again normalized to the initial electron energy, are plotted versus time for the case of $u_{b\perp} = 6v_{e0}$ in Fig. 2. In the case of the beam protons (upper plot), both bulk motion energy and thermal energy are included. During the simulation the beam proton energy drops by less than 1%, while the background proton energy (lower plot) rises by no more than about 10% (in the other simulations the perpendicular energies of the two ion species changed by even smaller amounts). In absolute terms the energy gained by background protons is very small compared to that lost by beam protons, with almost all the energy being transferred to electrons: we will demonstrate that the beam protons excite an instability which couples them efficiently to electrons.

In all the cases studied, electrons were energized in the direction perpendicular to the magnetic field. The upper plot in Fig. 3 shows, in more detail than Fig. 1, the time evolution of $\mathcal{E}_{\perp e}$ (once again normalized to its initial value) in the first 25 electron cyclotron periods of the simulation with $u_{b\perp} = 6v_{e0}$. The lower plot shows the time evolution of $\langle \varepsilon_0 E_x(x, t)^2 / 2 \rangle$, where ε_0 is the permittivity of free space, $E_x(x, t)$ is the x -component of the electric field, and the brackets $\langle \rangle$ denote a spatial average over the simulation box. In general, E_x is the dominant field component: since propagation in the x -direction only is represented, it follows that the waves excited are predominately electrostatic. Henceforth, the term “electric field” refers to the x -component. The field has a single value in each simulation box cell: the electrostatic field energy density $\langle \varepsilon_0 E_x(x, t)^2 / 2 \rangle$ is calculated by summing $\varepsilon_0 E_x(x, t)^2 / 2$ over the box and dividing by the number of cells. The energy density plotted in the lower frame of Fig. 3 is normalized to the perpendicular electron energy density at $\tilde{t} = 0$. The electron energy grows rapidly in two main phases, at $\tilde{t} \simeq 5$ and $\tilde{t} \simeq 14$, and then continues to grow at a slower rate. The field energy is greatly enhanced at times when the particle kinetic energy is growing rapidly: this suggests strongly that the fields are involved in particle acceleration. In the case of the wave energy burst at $\tilde{t} \simeq 5$, the field energy grows to a level comparable to the electron kinetic energy at that time. The energy of the burst occurring at $\tilde{t} \simeq 14$, on the other hand, is much lower than that of the electrons. Figure 4 shows the time evolution of $\mathcal{E}_{\perp e}$ and field energy in the simulation with $u_{b\perp} = 3.25v_{e0}$. The upper plot shows $\mathcal{E}_{\perp e}$ growing on a timescale comparable to the transit time of the simulation box through the shock foot. The lower plot shows

that electrostatic field activity is again correlated with electron acceleration. Figure 4 resembles the second of the two periods of wave growth in Fig. 3 (at $\tilde{t} \simeq 14$), in that the wave energy is small compared to the electron kinetic energy.

We now consider the distribution of wave amplitudes in wavenumber space. Figure 5 shows the time evolution of this distribution in the simulation with $u_{b\perp} = 6v_{e0}$. The grey scale shows the base 10 logarithm of the wave amplitude obtained by Fourier transforming in space the electric field of one of two counter-propagating waves excited by the ion beams. The start of the burst in wave energy in the lower plot of Fig. 3 at $\tilde{t} \simeq 3$ can be identified with the burst at $\tilde{k} \simeq 1.8$ in Fig. 5. This reaches an amplitude of 35 Vm^{-1} , generating a harmonic at $\tilde{k} \simeq 3.6$. When the peak amplitude is reached there is an increase in wave energy at $\tilde{k} < 1$. The frequency of this low \tilde{k} noise is close to the upper hybrid frequency $\omega_{uh} = (\omega_{pe}^2 + \Omega_e^2)^{1/2}$. Its appearance correlates with the maximum of the first wave burst at $\tilde{t} \simeq 5$ in the lower plot of Fig. 3, and with the strong increase of electron kinetic energy in the upper plot, suggesting that it arises from a redistribution of wave energy and changes in the electron distribution. After $\tilde{t} \simeq 8$, when the initial wave burst has disappeared, a more broadband perturbation is generated at $\tilde{k} \simeq 1.3$, the mean \tilde{k} decreasing with time. At $\tilde{t} = 14$ the wave amplitude peaks at about 16 Vm^{-1} : this is considerably lower than the peak electric field of 35 Vm^{-1} in the first burst, but nevertheless strong enough to generate two harmonics (at $\tilde{k} \simeq 2.6$ and $\tilde{k} \simeq 3.9$).

The corresponding plot for the simulation with $u_{b\perp} = 3.25v_{e0}$ is shown in Fig. 6. In this case instability occurs at discrete, regularly-spaced values of \tilde{k} . Waves with relatively high \tilde{k} ($\simeq 4$) are the first to be driven unstable: during the course of the simulation, the instability shifts to lower discrete wavenumbers. Broadband noise develops at $\tilde{k} < 1$, as in Fig. 5, but at a later time in the simulation ($\tilde{t} \simeq 35$). This appears to be associated with a more gradual evolution of the electron distribution than that which occurs in the simulation with $u_{b\perp} = 6v_{e0}$. The difference in temporal behaviour between Figs. 5 and 6 will be discussed later in this paper. Figures 5 and 6 show that in both simulations the plasma eventually stabilizes, on a timescale which depends on the beam velocity.

The dependence of wave amplitude on \tilde{k} and \tilde{t} when $u_{b\perp} = 5v_{e0}$ is qualitatively similar to Fig. 5: after an intense burst early in the simulation, a wave with slowly-varying amplitude is observed to cascade down in \tilde{k} as

time progresses. The growth rate of the first wave burst is 20% higher in the simulation with $u_{b\perp} = 6v_{e0}$ than it is in the simulation with $u_{b\perp} = 5v_{e0}$. In the former case, as mentioned above, the peak amplitude of the second burst is 16 Vm^{-1} , at $\tilde{k} = 1.25$ and $\tilde{t} = 14$; the corresponding figures for the simulation with $u_{b\perp} = 5v_{e0}$ are 12 Vm^{-1} , $\tilde{k} = 1.88$ and $\tilde{t} = 12$. The wave amplitude distribution in the simulation with $u_{b\perp} = 3.5v_{e0}$ is similar to Fig. 6: bursts of wave activity occur at discrete \tilde{k} , with the high \tilde{k} modes being driven unstable first.

In principle, it is also possible to determine the time evolution of wave amplitude as a function of $\tilde{\omega}$ and \tilde{k} . However, in order to obtain good frequency resolution it is necessary to average the amplitude over times longer than the electron acceleration timescale. Electrostatic waves in the electron cyclotron range propagating perpendicular to the magnetic field include, for example, electron Bernstein waves, whose dispersion relation depends on the electron distribution. Since this is rapidly evolving, it can be difficult to interpret observed distributions of wave amplitude in $\tilde{\omega}$ and \tilde{k} . However, we have found that the most strongly-growing waves in the simulations invariably have $\tilde{\omega} \simeq \tilde{k}u_{b\perp}/v_{e0}$: one can thus obtain the frequencies of the high intensity modes in Figs. 5 and 6 by multiplying \tilde{k} by $u_{b\perp}/v_{e0}$. By this means, it is straightforward to verify that the modes excited early in both simulations have $\tilde{\omega} \simeq 10$, and hence $\omega \simeq \omega_{pe}$.

3 Analysis of simulation results

Short-lived bursts of narrowband wave activity, correlated with rapid increases in electron kinetic energy, occur for all four values of $u_{b\perp}/v_{e0}$ considered above. These bursts appear throughout the simulations with $u_{b\perp} = 3.25v_{e0}$ and $u_{b\perp} = 3.5v_{e0}$; in the case of $u_{b\perp} = 5v_{e0}$ and $u_{b\perp} = 6v_{e0}$, they appear only at early times. In every case, the instability cascades to longer wavelengths in the course of the simulation. In order to compare the simulation results with those given by linear instability analysis (described in the next subsection), we determine growth rates for the first wave that interacts significantly with the electrons: in such cases one may assume that the electrons are still represented by a single Maxwellian velocity distribution with thermal speed v_{e0} . The simulations provide the wavenumber \tilde{k} of the unstable wave modes and the electric field amplitude E . The real frequencies $\tilde{\omega}$ of the unstable wave modes are assumed to be equal to $\tilde{k}u_{b\perp}/v_{e0}$. The

normalized growth rate γ/Ω_e is estimated by fitting an exponential to the plot of wave amplitude versus time during the period of most rapid growth in each simulation.

The results of this analysis are shown in Table 1. The symbol E_m denotes the maximum value of E during each simulation. In three of the four simulations there is a period of wave growth which can be described accurately as exponential. In each case, the growth rate falls to zero, and the wave decays: an example of this behaviour, for the case of $u_{b\perp} = 6v_{e0}$, is shown in Fig. 7, where wave amplitude (defined as in Figs. 5 and 6) at $\tilde{k} = 1.8$ is plotted versus normalized time. A possible reason for wave collapse (observed in all four simulations) will be discussed later in this paper. In the case of $u_{b\perp} = 3.25v_{e0}$, the mode referred to in Table 1 ($\tilde{k} \simeq 3.6$) is the second to be destabilized in that simulation. It appears to grow linearly rather than exponentially: for this reason, no figure is given for its growth rate. The first mode to be destabilized in this simulation, with $\tilde{k} \simeq 3.9$, does not grow to a large amplitude (compared to the noise level), and so it is difficult to determine its growth rate. Later in the paper we will present evidence of wave–wave interaction between the second mode excited ($\tilde{k} \simeq 3.6$) and the third mode excited ($\tilde{k} \simeq 3.3$), which may help to explain the linear growth of the latter.

Table 1. Parameters of highest intensity wave mode in each simulation.

$u_{b\perp}/v_{e0}$	\tilde{k}	$\tilde{\omega}$	γ/Ω_e	E_m (Vm ⁻¹)
6.0	1.8	10.8	0.24	35
5.0	2.15	10.7	0.2	23
3.5	3.3	11.6	0.05	2.5
3.25	3.6	11.7	–	1.6

Let us now examine whether the growth rates derived from the PIC simulations in Table 1 and Fig. 7 can be reproduced using linear stability theory.

3.1 Linear stability analysis

The appropriate dispersion relation for electrostatic, perpendicular–propagating waves with frequencies in the electron cyclotron range and above, excited by

an ion beam with a Maxwellian distribution in v_{\perp} , is (Melrose 1986)

$$1 - \frac{\omega_{pi}^2}{\omega^2} + \frac{2\omega_{pb}^2 [1 + \zeta_b Z(\zeta_b)]}{k^2 \delta u_{\perp}^2} - \frac{\omega_{pe}^2}{\omega} \frac{e^{-\lambda_e}}{\lambda_e} \sum_{\ell=-\infty}^{\infty} \frac{\ell^2 I_{\ell}}{\omega - \ell \Omega_e} = 0, \quad (2)$$

where: ω_{pi} , ω_{pb} are the background and beam ion plasma frequencies; Z is the plasma dispersion function, with argument $\zeta_b \equiv (\omega - k u_{b\perp})/k \delta u_{\perp}$; and I_{ℓ} is the modified Bessel function of the first kind of order ℓ with argument $\lambda_e \equiv T_e k^2 / (m_e \Omega_e^2)$. Both species of ion, having a much longer cyclotron period than the electrons, can be treated as unmagnetized particles on the timescales of interest here. Strictly speaking, there should be a term in Eq. (2) for each of the two proton beams, but since they have mean perpendicular speeds of opposite sign, and $\omega \simeq k u_{b\perp}$ is a prerequisite for wave-particle interaction, we need only consider one of them.

Solutions of Eq. (2) for complex ω in terms of real k can be readily obtained numerically, and compared with the simulation results in Table 1. In Figs. 8 and 9 $\tilde{\gamma} \equiv \text{Im}(\tilde{\omega})$ is plotted versus \tilde{k} for parameters corresponding to the initial conditions of the simulations with $u_{b\perp} = 6v_{e0}$ and $u_{b\perp} = 3.25v_{e0}$. In the former case it can be seen that strong instability drive occurs at $\tilde{k} \simeq 1.8$ with maximum growth rate $\tilde{\gamma} \simeq 0.25$, as observed early in the simulation (Fig. 5 and Table 1). The unstable real frequencies range from $\tilde{\omega} \simeq 8$ to $\tilde{\omega} \simeq 10.8$, and are thus clustered around the dimensionless electron plasma frequency ($\tilde{\omega} = 10$). The main instability appears to be essentially unaffected by cyclotronic effects: the growth rate does not depend on how close the frequency is to a cyclotron harmonic. There are, however, two much weaker instabilities at $\tilde{k} < 1$, which are narrowband in both \tilde{k} and $\tilde{\omega}$, the real frequencies lying just below the second and third cyclotron harmonics. In Fig. 9 instability occurs at $\tilde{k} \sim 3-4$, the corresponding real frequencies again clustering around ω_{pe} . In this case, however, the instability is modulated by cyclotronic effects, as in the simulation. Instability again occurs at $\tilde{k} < 1$, with real frequency $\tilde{\omega} \simeq 1.8$.

The mode appearing early in the simulation with $u_{b\perp} = 6v_{e0}$ arises from a two-stream instability (Buneman 1958). This can be driven by ions drifting relative to electrons in an unmagnetized plasma: it can also occur in a magnetized plasma, with ions drifting across the field, if ω_{pe}/Ω_e is sufficiently large, and the instability drive is sufficiently strong. Electrons as well as ions are then effectively unmagnetized and the appropriate dispersion relation is

(Melrose 1986)

$$1 - \frac{\omega_{pi}^2}{\omega^2} + \frac{2\omega_{pb}^2 [1 + \zeta Z(\zeta_b)]}{k^2 \delta u_{\perp}^2} + \frac{2\omega_{pe}^2 [1 + \zeta Z(\zeta_e)]}{k^2 v_{e0}^2} = 0, \quad (3)$$

where $\zeta_e \equiv \omega/kv_{e0}$. In the frequency régime of interest here ($\omega \simeq \omega_{pe}$), it can be shown easily that the background ion term in Eq. (3) can be neglected. Letting the thermal speeds of the two remaining species tend to zero, Eq. (3) reduces to

$$1 - \frac{\omega_{pb}^2}{(\omega - ku_{b\perp})^2} - \frac{\omega_{pe}^2}{\omega^2} = 0. \quad (4)$$

This differs slightly from the original two-stream dispersion relation analysed by Buneman (1958) in that the ions, rather than the electrons, have a finite drift speed. Buneman's equation becomes identical to Eq. (4) under the transformation $\omega \rightarrow ku_{b\perp} - \omega$: using this, we can infer from Buneman's analysis that Eq. (4) has a root $\omega = \omega_0 + i\gamma$, where real frequency ω_0 and growth rate γ are given approximately by

$$\omega_0 \simeq ku_{b\perp} - \omega_{pb}^{2/3} \omega_{pe}^{1/3} \cos^{4/3} \theta, \quad (5)$$

$$\gamma \simeq \omega_{pb}^{2/3} \omega_{pe}^{1/3} \cos^{1/3} \theta \sin \theta, \quad (6)$$

θ being a parameter whose value depends on $(ku_{b\perp} - \omega_{pe})/\omega_{pb}^{2/3} \omega_{pe}^{1/3}$ (Buneman 1958): it is straightforward to verify that the strongest wave growth occurs when $\theta = \pi/3$, which corresponds to $ku_{b\perp} = \omega_{pe}$. If $ku_{b\perp} \gg \omega_{pb}^{2/3} \omega_{pe}^{1/3} \cos^{4/3} \theta$, it follows from Eq. (5) that $\omega \simeq ku_{b\perp}$ and so the strongest drive occurs at $\omega \simeq \omega_{pe}$. However, since θ can have a range of values, the instability has finite bandwidth, extending to frequencies significantly below ω_{pe} . Solving the full Buneman dispersion relation [Eq. (4)] with $u_{b\perp} = 6v_{e0}$, we obtain results which are almost identical to those obtained from the magnetized dispersion relation [Eq. (2)], except, of course, that the cyclotronic features at $\tilde{k} < 1$ in Fig. 8 do not appear. Even in the case of $u_{b\perp} = 3.25v_{e0}$, Eq. (4) yields instability at about the same wavenumbers and frequencies as Eq. (2) [although the growth rates are somewhat higher in the case of Eq. (4)]. The essential difference between Figs. 8 and 9 is that the lower beam speed in the latter yields lower growth rates: when $\tilde{\gamma}$ is sufficiently small, the gyromotion of an electron in one wave growth period cannot be neglected, and the instability is modified by cyclotronic effects. However, the instability remains Buneman-like in character.

Further analysis of Eq. (2) indicates that the instability growth rate is a slowly-decreasing function of $\delta u_{\perp}/u_{b\perp}$: in the case of $u_{b\perp} = 6v_{e0}$, for example, the maximum growth rate is around $0.06\Omega_e$ when $\delta u_{\perp}/u_{b\perp} = 0.3$. The Buneman instability is thus robust, in the sense that its occurrence is not critically dependent on the velocity-space width of the reflected ion distribution. In any event, the values of $\delta u_{\perp}/u_{b\perp}$ used in our PIC simulations are broadly consistent with reflected beam ion distributions occurring in the hybrid simulations of Cargill & Papadopoulos (1988).

The instabilities at $\tilde{k} < 1$ in Figs. 8 and 9 arise from the interaction of a beam mode ($\omega \simeq ku_{b\perp}$) with electron Bernstein modes. The existence of such instabilities can be inferred analytically by taking the limit of Eq. (2) for cold beam and background protons:

$$1 - \frac{\omega_{pi}^2}{\omega^2} - \frac{\omega_{pb}^2}{(\omega - ku_{b\perp})^2} - \frac{\omega_{pe}^2}{\omega} \frac{e^{-\lambda_e}}{\lambda_e} \sum_{\ell=-\infty}^{\infty} \frac{\ell^2 I_{\ell}}{\omega - \ell\Omega_e} = 0. \quad (7)$$

In the absence of the proton beam term, Bernstein mode solutions of Eq. (7) have frequencies which approach $\ell\Omega_e$ ($\ell = 1, 2, 3, \dots$) as $k \rightarrow \infty$ and $(\ell + 1)\Omega_e$ as $k \rightarrow 0$ (the long wavelength limit is different for frequencies equal to or greater than the upper hybrid frequency ω_{uh} , which in the case of the simulations presented in Sect. 2 is about $10\Omega_e$). When $n_b \neq 0$, approximate analytical solutions of Eq. (7) can be obtained by setting $\omega = ku_{b\perp} + i\gamma$ and solving perturbatively for γ in certain limits. For example, letting $\lambda_e \rightarrow 0$ and assuming that ω does not lie close to a harmonic of Ω_e , we obtain

$$\frac{\gamma}{\Omega_e} \simeq \left(\frac{m_e}{m_p}\right)^{1/2} \left(\frac{n_b}{n_e}\right)^{1/2} \left(\frac{\omega^2}{\Omega_e^2} - 1\right)^{1/2}. \quad (8)$$

Instability, corresponding to real γ , thus requires $\omega > \Omega_e$. For ω sufficiently close to $\ell\Omega_e$, the electron term in Eq. (7) is dominated by the ℓ -th harmonic, and instead of Eq. (8) we obtain

$$\frac{\gamma}{\Omega_e} \simeq \frac{\omega}{\Omega_e} \left(\frac{m_e}{m_i}\right)^{1/2} \left(\frac{n_b}{n_e}\right)^{1/2} \frac{\lambda_e e^{\lambda_e}}{(\ell I_{\ell})^{1/2}} \left(1 - \frac{\ell\Omega_e}{\omega}\right)^{1/2}. \quad (9)$$

Numerical solutions of Eq. (2) for $\omega \sim \Omega_e$ are broadly consistent with Eqs. (8) and (9). In both these cases the growth rate scales as $(m_e/m_p)^{1/2}$: in contrast, the Buneman growth rate [Eq. (6)] scales as $(m_e/m_p)^{1/3}$. This helps to explain the fact that in Figs. 8 and 9 the Buneman instability

is stronger than the lower frequency Bernstein instability. It should also be noted that most astrophysical plasmas have a higher ratio of electron plasma frequency to gyrofrequency than that assumed in the simulations ($\omega_{pe}/\Omega_e = 10$). Normalized to Ω_e , the Buneman growth rate scales as ω_{pe}/Ω_e , and so the instability is less likely to be modified by cyclotronic effects when $\omega_{pe}/\Omega_e > 10$. The electron Bernstein modes exist because T_e is finite: thus, the transition from Buneman to electron Bernstein instability depends on the value of v_{e0} . If the initial electron temperature in the simulations had been lower than 80 eV, the Buneman instability would, again, have been affected to a lesser extent by cyclotronic effects.

3.2 Nonlinear effects

Figure 1 shows strong increases in electron kinetic energy perpendicular to the magnetic field in all four simulations. There is a strong correlation between acceleration and wave excitation via the Buneman instability (Figs. 3 and 4). Although such waves can energize electrons via Landau damping (Papadopoulos 1988), one would expect this process to be of limited effectiveness when, as in the present case, the waves are propagating perpendicular to the magnetic field and have a growth rate which is comparable to or less than Ω_e . It is likely therefore that the very strong electron acceleration observed in the simulations is due at least in part to nonlinear processes.

As noted previously, the second mode to be excited in the simulation with $u_{b\perp} = 3.25v_{e0}$ does not undergo an exponential growth phase. Figure 10 shows the time evolving wave amplitudes of this mode, at $\tilde{k} = 3.6$ (upper plot), and the third mode to be excited, at $\tilde{k} = 3.3$ (lower plot). The amplitude at $\tilde{k} = 3.6$ grows linearly up to $\tilde{t} \simeq 27$, and then collapses. The amplitude at $\tilde{k} = 3.3$ grows exponentially from $\tilde{t} \simeq 7$ to $\tilde{t} \simeq 14$, with $\gamma/\Omega_e \simeq 0.04$: this is close to the growth rate at $\tilde{k} = 3.3$ found by linear stability analysis (Fig. 9). The amplitude remains constant until $\tilde{t} \simeq 27$, and then grows linearly until $\tilde{t} \simeq 35$. The linear growth of the wave at $\tilde{k} = 3.3$ thus correlates strongly with the collapse of the wave at $\tilde{k} = 3.6$: this suggests wave-wave coupling. The linear growth of the wave at $\tilde{k} = 3.6$ may, in turn, be correlated with the decay of the first mode to be excited, at $\tilde{k} \simeq 3.9$ (see Fig. 6): the latter has the highest growth rate of waves in this range, according to linear stability analysis (Fig. 9).

We now consider specific nonlinear processes which may be occurring in the simulations. Karney (1978) examined the nonlinear interaction of large

amplitude electrostatic lower hybrid waves with ions. The particle motion is described by a normalized Hamiltonian

$$h = \frac{1}{2}(p_x + y)^2 + \frac{1}{2}p_y^2 - \alpha \sin(y - \mu t), \quad (10)$$

where: $\hat{\mathbf{y}}$, $\hat{\mathbf{z}}$ are, respectively, the wave propagation and magnetic field directions; the canonical momentum components p_x, p_y are normalized to $m\Omega/k$, where m and Ω are particle mass and gyrofrequency; the position variable y is normalized to $1/k$; μ is wave frequency in units of Ω ; and α is given by

$$\alpha = \frac{E/B}{\Omega/k}, \quad (11)$$

E being the wave electric field amplitude. The first two terms in the Hamiltonian describe the motion of the particle in the magnetic field; the third term arises from the electrostatic wave. The system can be regarded as consisting of two harmonic oscillators: one associated with the particle gyromotion around B , the other with the wave. These oscillators are coupled by the parameter α , the value of which determines the extent to which the system phase space is regular or stochastic. Karney (1978) solved the Hamiltonian equations corresponding to Eq. (10) for a range of initial conditions, plotting normalized Larmor radius $r = kv_{\perp}/\Omega$ versus wave phase angle ϕ at the particle's position, for successive transits of the particle through a particular gyrophase angle. Particle trajectories were thus represented as discrete sets of points in (r, ϕ) space. For sufficiently small values of α , all particles have regular orbits, represented by smooth curves in (r, ϕ) space, spanning all values of ϕ and with only small variations in r . When α exceeds a certain threshold α_0 , "islands" appear in (r, ϕ) space, within which particle trajectories are confined. Further increases in α lead to the formation of more islands, which cause the phase space to become stochastic: at sufficiently large $\alpha > \alpha_c$, the system phase space is completely stochastic, with no regular orbits remaining. The initial electron distributions in our simulations decrease monotonically in v_{\perp} : in such cases stochasticity in phase space tends to favour particle diffusion to larger velocities, i.e. acceleration.

Karney (1978) obtained the following analytical estimate for α_0 :

$$\alpha_0 = \left| \frac{r(\omega/\Omega - \ell)}{\ell(d/dr)J_{\ell}(r)} \right|, \quad (12)$$

where $\ell\Omega$ is the cyclotron harmonic closest to ω and J_ℓ is the Bessel function of order ℓ . Karney's analysis does not explicitly involve a particular type of wave or particle, or a specific particle distribution function. The results can thus be applied to the case of electrons interacting with electrostatic waves excited by the Buneman instability, in which case $m = m_e$ and $\Omega = \Omega_e$. Combining Eqs. (11) and (12) and using the identity

$$\frac{d}{dr} J_\ell(r) = \frac{\ell}{r} J_\ell(r) - J_{\ell+1}(r), \quad (13)$$

we infer that the critical electric field $E = E_i$ for island formation in (r, ϕ) space is

$$E_i = \frac{v_\perp B_0 |\mu - \ell|}{\ell \left| \frac{\ell}{r} J_\ell(r) - J_{\ell+1}(r) \right|}. \quad (14)$$

In general, it is not possible to determine analytically an expression for the electric field amplitude $E = E_c$ corresponding to $\alpha = \alpha_c$, above which the phase space becomes completely stochastic. Karney obtained an empirical expression for α_c , based on numerical calculations with particular values of μ and r , which may not be applicable to the simulation results discussed here. However, island formation is a first step in the destruction of regularity in the system phase space, and E_i can be regarded as an approximate threshold for stochasticity: electric field amplitudes which are significantly higher than E_i will convert regular orbits at a particular v_\perp into stochastic ones.

In the cases $u_{b\perp} = 5v_{e0}$ and $6v_{e0}$, linear stability analysis indicates that wave growth occurs across a range of frequencies $\omega \sim \omega_{pe}$, which includes cyclotron harmonics: in such cases $\mu = \ell$, and any non-zero wave amplitude E will cause islands to be formed. In the case of the lower two beam speeds, the unstable frequencies lie between cyclotron harmonics, and E_i is thus always finite. Table 2 lists the values of E_i derived from Eq. (14) that are required for comparison with the highest intensity wave mode excited in each simulation. The actual peak electric fields of these waves are given in Table 1.

Table 2. Values calculated for E_i using the wave parameters given in Table 1.

v_{\perp}/v_{e0}	closest ℓ	$(\mu - \ell)$	kv_{\perp}/Ω_e	E_i (Vm^{-1})
6.0	11	0.2	10.8	1.8
5.0	11	0.3	10.7	2.3
3.5	12	0.4	11.6	2.1
3.25	12	0.3	11.7	1.4

Comparing Tables 1 and 2, we see that waves are excited with amplitudes exceeding E_i in all four cases. For the simulation with $u_{b\perp} = 3.25v_{e0}$, $E/E_i \simeq 1.1$. This ratio rises to 1.2 for $u_{b\perp} = 3.5v_{e0}$, 10 for $u_{b\perp} = 5v_{e0}$, and 19 for $u_{b\perp} = 6v_{e0}$. In the latter two cases, as we have seen, waves are excited with $\omega = \ell\Omega_e$, for which island formation occurs regardless of the value of E . The fact that $E_m/E_i \gg 1$ at higher values of $u_{b\perp}$ indicates that the phase space in these simulations is characterized by strong stochasticity. The waves rapidly collapse, however, soon after the onset of strong electron acceleration. In the other two simulations, the peak amplitudes are only just sufficient for island formation to occur, and it is likely that little stochasticity occurs in the system phase space. The waves excited in these simulations decay more gradually than those produced at higher $u_{b\perp}$.

We now consider possible explanations for two of the results noted above: the sharp rise in wave amplitude when the beam speed is raised from $3.5v_{e0}$ to $5v_{e0}$; and wave collapse, which occurs in all four simulations but is particularly rapid in the two simulations with higher $u_{b\perp}$. As far as the dependence of wave amplitude on $u_{b\perp}$ is concerned, the first point to note is that the unstable waves all satisfy $\omega \simeq u_{b\perp}k$. In each simulation the total number of computational particles is, of course, finite, the Maxwellian electron velocity distribution being initialized up to $v_{\perp} \simeq 5v_{e0}$. Thus, the beams with $u_{b\perp} = 5v_{e0}$ and $6v_{e0}$ excite waves with phase velocities exceeding the velocity of any electron in the simulation: this is not so in the simulations with $u_{b\perp} = 3.25v_{e0}$ and $3.5v_{e0}$. The minimum electron velocity required for wave-particle interactions is the phase velocity of the wave: thus, only the slow beams can excite waves capable of interacting with electrons at the start of the simulations. The wave-particle interaction results in electron acceleration, the energy for this being drawn from the wave. This energy loss may account for the relatively low peak electric field amplitudes of waves excited by the slow beams.

The waves generated by the fast beams, on the other hand, cannot initially interact resonantly with the electron population, and so their amplitudes can grow to levels much higher than E_i . Sufficiently high wave amplitudes can activate a second acceleration mechanism, which arises from particle trapping in the wave electric field (Karney 1978): electrons with an initially monotonic decreasing distribution are re-distributed uniformly within the trap, the result being a net increase in kinetic energy. The wave can trap electrons with perpendicular velocities differing from the wave's phase velocity by up to v_{tr} , where

$$v_{\text{tr}} = \sqrt{\frac{eE}{mk}}. \quad (15)$$

For $u_{b\perp} = 5v_{e0}$, the maximum electric field is 23 Vm^{-1} and the wavenumber k is $5.7 \times 10^{-3} \times 2\pi \text{ m}^{-1}$. In this case $v_{\text{tr}} = 1.1 \times 10^7 \text{ ms}^{-1} \simeq 2.8v_{e0}$. For $u_{b\perp} = 6v_{e0}$, the maximum field is 35 Vm^{-1} and $k = 4.8 \times 10^{-3} \times 2\pi \text{ m}^{-1}$, so that $v_{\text{tr}} = 1.4 \times 10^7 \text{ ms}^{-1} \simeq 3.8v_{e0}$. The waves excited in the simulations with higher beam speeds can thus trap electrons deep within the electron thermal population: a large number of electrons can then be pre-accelerated to velocities comparable to the wave's phase velocity, with further acceleration taking place via the stochastic mechanism discussed previously. A two-stage process of this type was proposed by Karney (1978). Whereas the first burst of wave activity in Fig. 3 contained more energy than the electron population, the energy in the second burst was much lower than the perpendicular electron kinetic energy by that stage of the simulation. This may have been due to the first burst resulting in trapped electrons populating the region of phase space at $v_{\perp} \simeq u_{b\perp}$, via the trapping mechanism. The perpendicular electron velocity distribution would then be considerably broader than it was initially, with an effective thermal speed $v_e > v_{e0}$. The beam distribution, on the other hand, did not change significantly during the simulation (see Fig. 2), and so $u_{b\perp}/v_e < u_{b\perp}/v_{e0}$. The situation would then be similar to that of the simulations with lower beam speeds, in which electrons can immediately absorb energy from waves with $\omega \simeq ku_{b\perp}$, and one would expect any subsequent wave burst to have a peak energy much lower than that of the electron population, as observed.

With regard to the second observation, wave collapse, it is interesting to note that in every case the wave amplitude falls to a level well below E_i : intuitively, one would have expected the waves to cease interacting with electrons, and hence to reach a steady-state level, when their amplitudes had

fallen below E_i . The collapse may be associated with changes in the dispersion characteristics of the wave mode resulting from strong particle acceleration. Karney (1978) justified his Hamiltonian approach by considering only stochastic regions of phase space, at particle speeds (and hence wave phase speeds) greatly exceeding v_{e0} . The stochastic regions thus lie in the high velocity tail of the initial Maxwellian electron distribution, and most electrons are not initially affected by the wave–particle interaction. However, in the simulations with $u_{b\perp} = 5v_{e0}, 6v_{e0}$ the reduction in $u_{b\perp}/v_e$ noted above means that perpendicular electron speeds are no longer small compared to the wave phase speed, and we find that there is a transition from the pure Buneman instability shown in Fig. 8 to the more complicated instability shown in Fig. 9: the latter, as we have discussed, has a Buneman–like envelope, but also has cyclotronic features, and in fact linear stability analysis shows that the variation of ω with k in this case is characteristic of the beam/electron Bernstein mode discussed in Subsect. 3.1. As $u_{b\perp}/v_e$ falls, the maximum growth rate drops considerably, but remains positive if the electrons retain a Maxwellian distribution. However, as we now demonstrate, the electron distributions occurring in the simulations are often far from Maxwellian.

3.3 Particle distributions

From the simulation results we have evaluated the distribution of perpendicular electron speeds $f(v_\perp)$, defined such that

$$\int_0^\infty f(v_\perp) dv_\perp = N_e, \quad (16)$$

where N_e is the total number of electrons in the simulation. With this definition, a Maxwellian velocity distribution is of the form $v_\perp e^{-v_\perp^2/2v_e^2}$, decreasing monotonically for $v_\perp > v_e$. One advantage of plotting a distribution in this way is that the thermal speed of a Maxwellian can be readily identified graphically, being the speed at which $df/dv_\perp = 0$. In Fig. 11 $f(v_\perp)$ is plotted for $\tilde{t} = 0, 45, 90$ and 135 in the simulations with $u_{b\perp} = 3.25v_{e0}$ (dash–dotted curves) and $u_{b\perp} = 3.5v_{e0}$ (solid curves). The two curves are identical for $\tilde{t} = 0$, since the same initial electron temperature is used in all four simulations. At $\tilde{t} = 45$ the proton beams have generated hot electron tails, peaking at $v_\perp \simeq 4v_{e0}$ ($u_{b\perp} = 3.25v_{e0}$) and $v_\perp \simeq 6v_{e0}$ ($u_{b\perp} = 3.5v_{e0}$). The maximum electron speeds in the two cases are $7v_{e0}$ ($u_{b\perp} = 3.25v_{e0}$) and $10v_{e0}$ ($u_{b\perp} = 3.5v_{e0}$). At $\tilde{t} = 90$ the slower beam has produced a local maximum

in $f(v_\perp)$ at $5v_{e0}$, and a high velocity cutoff at $10v_{e0}$. The local maximum has become less pronounced at $\tilde{t} = 135$. In the case of $u_{b\perp} = 3.5v_{e0}$ a local maximum can be seen at $\tilde{t} = 45$: by $\tilde{t} = 90$, however, the distribution is monotonic decreasing above a speed only slightly higher than the initial thermal speed. By the end of this simulation $f(v_\perp)$ extends up to $12v_{e0}$.

In Fig. 12 $f(v_\perp)$ is shown for $\tilde{t} = 0, 20, 40$ and 70 in the simulations with $u_{b\perp} = 5v_{e0}$ (dash-dotted curves) and $u_{b\perp} = 6v_{e0}$ (solid curves). At $\tilde{t} = 20$ the two distributions have local maxima at $v_\perp \gg v_{e0}$, as in the second frame of Fig. 11: for $u_{b\perp} = 5v_{e0}$ the distribution peaks locally at $v_\perp \simeq 10v_{e0}$ and falls to zero at $v_\perp \simeq 18v_{e0}$. The corresponding figures at the same stage of the simulation with $u_{b\perp} = 6v_{e0}$ are $12v_{e0}$ and $22v_{e0}$. By $\tilde{t} = 40$, the local maxima still exist and, indeed, the bumps-on-tail containing these maxima actually comprise most of the electron population in both cases. By this time the high velocity tails extend to $v_\perp \simeq 25 - 30v_{e0}$. Local maxima close to the original thermal speeds v_{e0} still exist, but these have disappeared by $\tilde{t} = 70$. The strong wave bursts in these simulations occur before $\tilde{t} = 20$: after this time, a weaker, more broadband instability occurs at lower \tilde{k} , but still with $\tilde{\omega} \simeq \tilde{k}u_{b\perp}/v_{e0}$. To model this instability, we can approximate the solid curve at $\tilde{t} = 20$ in Fig. 12 by superposing two Maxwellians, with thermal velocities $v_{ec} = v_{e0}$, $v_{eh} = 10v_{e0}$ and densities $n_{ec} = 0.38n_e$, $n_{eh} = 0.62n_e$. The solid curve in Fig. 13 shows the true distribution at $\tilde{t} = 20$; the dashed curve shows the bi-Maxwellian fit to this distribution. The match is not exact, but is close enough to suggest that we can model wave excitation at this stage of the simulation by solving a modified version of the dispersion relation [Eq. (2)], with the parameters of the dashed curve defining the electron distribution. Results indicate an electron Bernstein instability with maximum growth rate $\gamma \simeq 0.08\Omega_e$ at $\tilde{k} \simeq 1.4$, $\tilde{\omega} \simeq 8.2\Omega_e$: the wavenumbers are consistent with those of fluctuations appearing at $\tilde{t} \geq 20$ in Fig. 5.

The electron distributions at $\tilde{t} = 70$ in the simulations with $u_{b\perp} = 5v_{e0}$ and $u_{b\perp} = 6v_{e0}$ (Fig. 12) can both be approximated by single Maxwellians, respectively with $v_e \simeq 8v_{e0}$ and $v_e \simeq 12v_{e0}$. The proton beam-excited Buneman instability can thus produce electron distributions whose perpendicular thermal speeds exceed the velocities of the ion beams which produced them. The fastest-moving electrons have $v_\perp \gg u_{b\perp}$. This phenomenon, observed in all four simulations, is further strong evidence for nonlinear processes playing a role in electron acceleration: in the quasi-linear limit, unmagnetized electrons of a particular speed v_0 can only interact with waves whose phase speed equals v_0 , and the range of wave phase speeds is determined in turn by the

ion beam speeds. In the case of $u_{b\perp} = 6v_{e0}$, the final electron temperature is about 11.5 keV: this is easily sufficient to account for thermal X-ray emission observed from SNRs such as Cas A (Papadopoulos 1988). Individual electron energies up to several tens of keV were obtained in the simulations.

4 Conclusions and Discussion

Using particle-in-cell (PIC) simulations and linear stability theory, we have shown that electrostatic waves in the electron plasma range, excited by ions reflected from a high Mach number perpendicular shock, can effectively channel the free energy of the shock into electrons. Such shocks are known to be associated with SNRs, and the processes investigated in this paper may thus help to account for both X-ray thermal bremsstrahlung and the creation of “seed” electron populations for diffusive shock acceleration to MeV and GeV energies in such objects. The simulation results provide confirmation of a proposal by Papadopoulos (1978) and Cargill & Papadopoulos (1978) that streaming between reflected ions and upstream electrons can give rise to a strong Buneman instability. Whereas these authors assumed that the sole effect of the Buneman instability would be electron heating, the PIC simulations show acceleration – the development of strongly non-Maxwellian, anisotropic features in electron velocity distributions. The maximum electron velocities are considerably higher than those expected on the basis of quasi-linear theory: this implies that nonlinear wave-particle interactions are contributing to the acceleration. When the beam speed is greater than about four times the initial electron thermal speed, thermalization of the electron population is observed after saturation of the Buneman instability, the final electron temperature being of the order of 10–12 keV.

It is possible that the acceleration process identified in this paper may be relevant to oblique shocks as well as strictly perpendicular ones. A necessary requirement is the presence of reflected ion beams, which have been observed (Sckopke et al. 1983) upstream of both quasi-parallel and quasi-perpendicular regions of the Earth’s bow shock (the term “quasi-perpendicular” is conventionally used to describe a shock at which the angle θ_{Bn} between the shock normal and the upstream magnetic field is greater than 45°). Leroy et al. (1982) used a hybrid code to simulate ion reflection at shocks with a range of values of θ_{Bn} , finding very similar results for $\theta_{Bn} = 80^\circ$ and $\theta_{Bn} = 90^\circ$. They inferred from this that hybrid sim-

ulations which use strictly perpendicular geometry may be compared with observational data of quasi-perpendicular shocks. Additional necessary requirements for electron acceleration via the Buneman instability are that the projection of the reflected ion beam velocity onto the plane perpendicular to the upstream field exceed the upstream electron thermal speed, and that the plasma be weakly magnetized, in the sense that $\omega_{pe} > \Omega_e$. When these conditions are satisfied locally, the Buneman instability will occur. Whether this instability is sufficient to produce significant electron energization at oblique shocks as well as perpendicular and nearly perpendicular ones remains to be demonstrated, however. In the simulations presented in this paper, acceleration occurred on timescales shorter than an ion cyclotron period. It was not necessary to represent the shock foot structure, since this has dimensions of the order of a reflected ion Larmor radius, and for this reason θ_{Bn} is not explicitly a parameter in our model. Leroy et al. (1982) have noted, however, that extrapolations of results obtained for nearly perpendicular shocks ($80^\circ \leq \theta_{Bn} \leq 90^\circ$) to more oblique shocks should be treated with caution, since the physical processes governing the shock structure can be expected to change as θ_{Bn} is reduced.

The simulation results and our analysis of them suggest that the damping of waves in the electron plasma range at perpendicular SNR shocks could provide a solution to the cosmic ray electron injection problem. Although wave-particle interactions at such shocks have been invoked previously in this context (Galeev 1984; Papadopoulos 1988; Cargill & Papadopoulos 1988; Galeev et al. 1995; McClements et al. 1997), the simulation results presented here contain several new features. These include: the acceleration, rather than heating, of electrons via the Buneman instability; the acceleration of electrons to speeds exceeding those of the shock-reflected ions producing the instability; and strong acceleration of electrons perpendicular to the magnetic field. The wave-particle mechanisms proposed by Galeev (1984) and McClements et al. (1997) gave rise to electron acceleration primarily along the magnetic field. Diffusive shock acceleration, which is probably essential for the production of ultra-relativistic electrons, can occur when the electrons have magnetic rigidities comparable to those of ions flowing into the shock. Since, however, the diffusive shock mechanism requires electrons to be rapidly scattered, its efficacy does not depend sensitively on the initial pitch angle distribution. The geometry of the simulations described here (\mathbf{B} perpendicular to the one space dimension) excludes the possibility of acceleration by electrostatic waves along the parallel direction. The present

model is complementary to those of Galeev (1984), Galeev et al. (1995) and McClements et al. (1997), in that it provides an alternative means of energizing electrons at perpendicular shocks. At a real SNR shock, perpendicular acceleration via the Buneman instability and parallel acceleration via wave excitation at $\omega < \Omega_e$ are both likely to occur. PIC simulations in two space dimensions would make it possible to assess quantitatively the relative contributions of these two types of instability to electron energization under a range of conditions.

We discuss finally our neglect of the finite plasma current present in the foot region of perpendicular shocks. This approximation does not appear to have introduced unrealistic elements into our simulation results, except insofar as the absence of a finite drift between the electrons and background protons removes a possible source of drive for the ion acoustic instability, invoked as one of the electron heating mechanisms in the model of Papadopoulos (1988). However, if the background protons and electrons flowing into the shock foot are approximately isothermal, it seems unlikely that any instability excited by their relative streaming could result in a significant transfer of energy from one species to the other. Another possibility is that ion acoustic instability could result from the streaming of beam protons relative to electrons. This would require, however, the electron temperature to be extremely large compared to the beam proton temperature (ion Landau damping strongly suppresses the instability when the temperatures are equal): even in the simulation which produced an effective electron temperature of 80 times the initial temperature, this condition was not satisfied. Thus, the simulation parameters were such that the ion acoustic instability could not occur. It is interesting to note, however, that the curve corresponding to $u_{b\perp} = 6v_{e0}$ in the lower frame of Fig. 1 bears a certain resemblance to a curve in Fig. 5 of Papadopoulos' 1988 paper (Fig. 5), showing schematically the predicted variation of electron temperature with distance in a quasi-perpendicular shock foot: in both cases, there is a very rapid rise in the total electron energy, resulting from strong Buneman instability, followed by a more gradual rise, which coincides in the simulations with the excitation of electron Bernstein modes. The latter may play a role in the simulations which is similar to that of the ion acoustic mode in the model of Papadopoulos.

Acknowledgements. This work was supported by the Commission of the European Communities, under TMR Network Contract ERB-CHRXCT98-0168, by the UK Department of Trade and Industry, and by EURATOM. S.

C. Chapman was supported by a PPARC lecturer fellowship.

REFERENCES

- Achterberg A., Blandford R.D., Reynolds S.P., 1994, *A&A* 281, 220
Anderson K.A., Lin R.P., Martel F., Lin C.S., Parks G.K., Reme H., 1979, *Geophys. Res. Lett.* 6, 401
Axford W.I., Leer E., Skadron G., 1977, in: *Proceedings of the 15th International Cosmic Ray Conference*, Christov C.Y. (ed.), Central Research Institute for Physics, Budapest, vol. 11, 132
Bell A.R., 1978, *MNRAS* 182, 147
Bessho N., Ohsawa Y., 1999, *Phys. Plasmas* 6, 3076
Blandford R.D., Ostriker J.P., 1978, *ApJ* 221, L29
Buneman O., 1958, *Phys. Rev. Lett.* 1, 8
Cargill P.J., Papadopoulos K., 1988, *ApJ* 329, L29
Denavit J., Kruer W.L., 1980, *Comments Plasma Phys. Cont. Fusion* 6, 35
Devine P., 1995, Ph.D. Thesis, University of Sussex
Galeev A.A., 1984, *Sov. Phys. JETP* 59, 965
Galeev A.A., Malkov M.A., Völk H.J., 1995, *J. Plasma Phys.* 54, 59
Karney C.F.F., 1978, *Phys. Fluids* 21, 1584
Kirk J.G., Heavens A.F., 1989, *MNRAS* 239, 995
Koyama K., Petre R., Gotthelf E.V., Hwang, U., Matsuura M., Ozaki M., Holt S.S., 1995, *Nature* 378 255
Krymsky G.F., 1977, *Dokl. Akad. Nauk. SSSR* 234, 1306
Laming J.M., 1998, *ApJ* 499, 309
Leroy M.M., Winske D., Goodrich C.C., Wu C.S., Papadopoulos, K., 1982, *J. Geophys. Res.* 87, 5081
Levinson A., 1996, *MNRAS* 278, 1018
McClements K.G., Bingham R., Su J.J., Dawson J.M., Spicer D.S., 1993, *ApJ* 409, 465
McClements K.G., Dendy R.O., Bingham R., Kirk J.G., Drury L.O'C., 1997, *MNRAS* 291, 241
Melrose D.B., 1986, *Instabilities in Space and Laboratory Plasmas*, Cambridge University Press
Papadopoulos K., 1988, *Ap&SS* 144, 535
Pohl M., Esposito J.A., 1998, *ApJ* 507, 327
Quest K.B., 1986, *J. Geophys. Res.* 91, 8805

Sckopke N., Paschmann G., Bame S.J., Gosling J.T., Russell C.T., 1983, J. Geophys. Res. 88, 6121
Willingale R., West R.G., Pye J.P., Stewart G.C., 1996 MNRAS 278, 479
Woods L.C., 1969, J. Plasma Phys. 3, 435

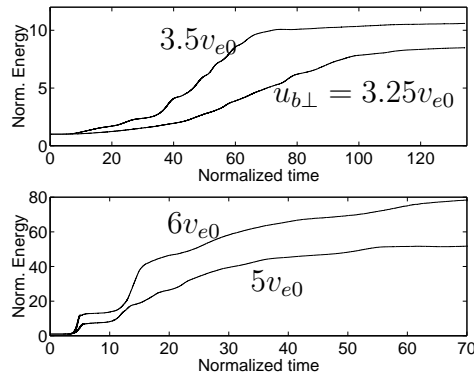


Figure 1: Total electron perpendicular kinetic energy, normalized to its initial value, versus simulation time in electron cyclotron periods $2\pi/\Omega_e$, for several values of $u_{b\perp}/v_{e0}$. Energy transfer to electrons is much more rapid at $u_{b\perp} = 5v_{e0}$ and $u_{b\perp} = 6v_{e0}$ than it is at lower beam speeds.

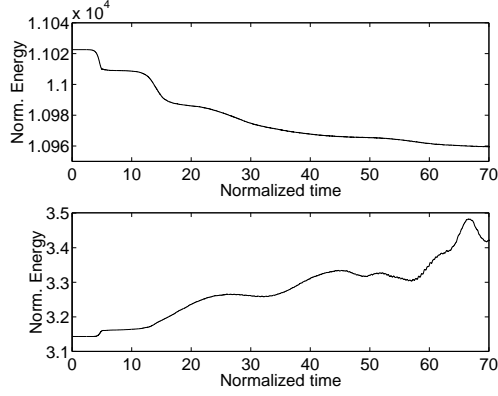


Figure 2: Normalized beam proton (upper plot) and background proton (lower plot) perpendicular kinetic energies (both normalized to initial electron thermal energy) versus simulation time for the simulation with $u_{b\perp} = 6v_{e0}$. The beam proton energy drops by less than 1%; the background proton energy increases by approximately 10%.

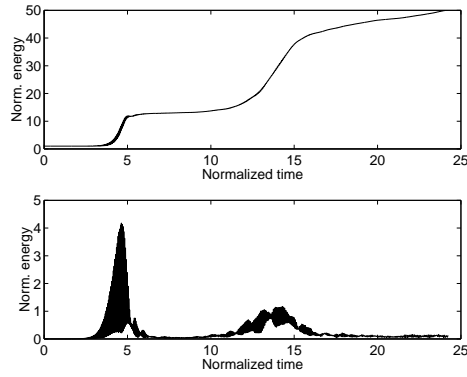


Figure 3: Time evolution of perpendicular electron kinetic energy (upper plot) and electrostatic field energy (lower plot) in the simulation with $u_{b\perp} = 6v_{e0}$.

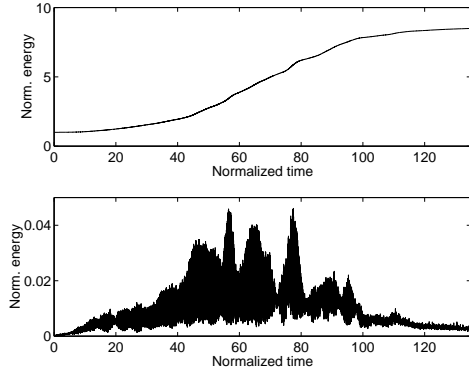


Figure 4: Time evolution of perpendicular electron kinetic energy (upper plot) and electrostatic field energy (lower plot) in the simulation with $u_{b\perp} = 3.25v_{e0}$.

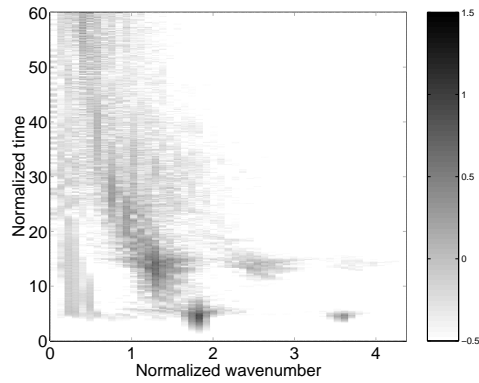


Figure 5: Base 10 logarithm of electric field amplitude (Vm^{-1}) versus \tilde{k} and \tilde{t} in the simulation with $u_{b\perp} = 6v_{e0}$.

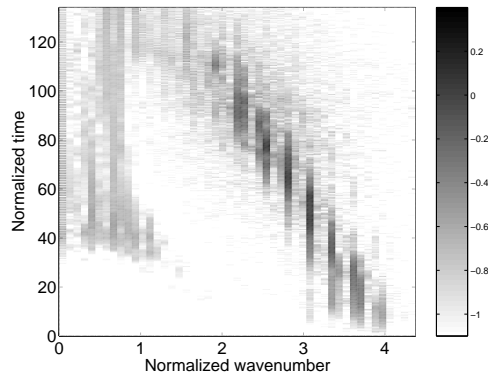


Figure 6: Base 10 logarithm of electric field amplitude (Vm^{-1}) versus \tilde{k} and \tilde{t} in the simulation with $u_{b\perp} = 3.25v_{e0}$.

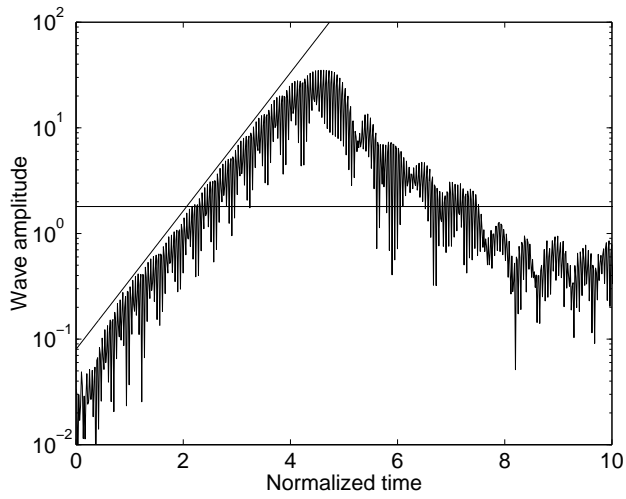


Figure 7: Time evolution of electric field amplitude (Vm^{-1}) at $\tilde{k} = 1.8$ after the onset of instability in the simulation with $u_{b\perp} = 6v_{e0}$. The horizontal line is E_i for this wave; the diagonal line shows an exponential fit to the growth rate with $\gamma/\Omega_e = 0.24$.

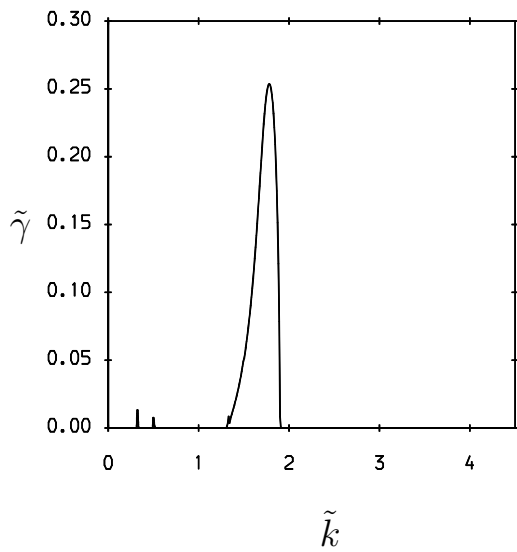


Figure 8: Predicted linear growth rates of waves with $\omega > \Omega_e$ when the beam speed is $6v_{e0}$. The other dispersion relation parameters correspond to the initial conditions of all four simulations.

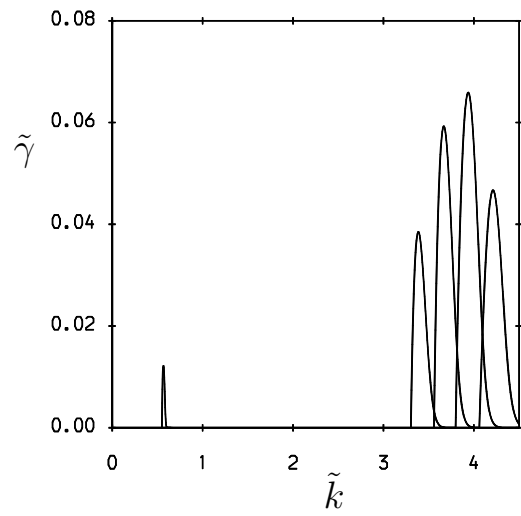


Figure 9: Predicted linear growth rates of waves with $\omega > \Omega_e$ when the beam speed is $3.25v_{e0}$.

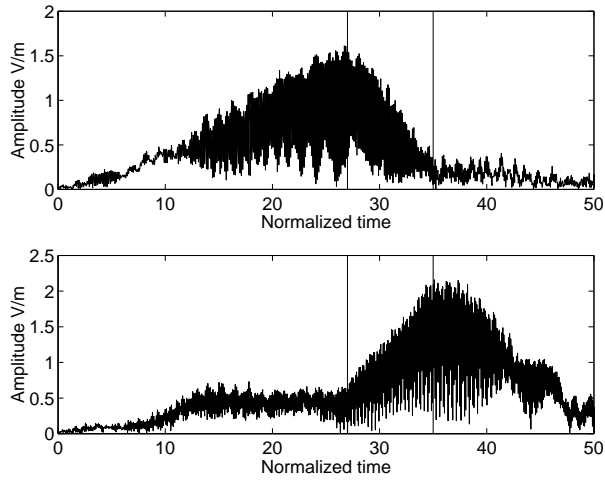


Figure 10: Time evolution of electric field amplitude (Vm^{-1}) at $\tilde{k} = 3.6$ (upper plot) and $\tilde{k} = 3.3$ (lower plot) after the onset of instability in the simulation with $u_{b\perp} = 3.25v_{e0}$. The vertical lines indicate a period in which there is an anti-correlation between the two wave amplitudes.

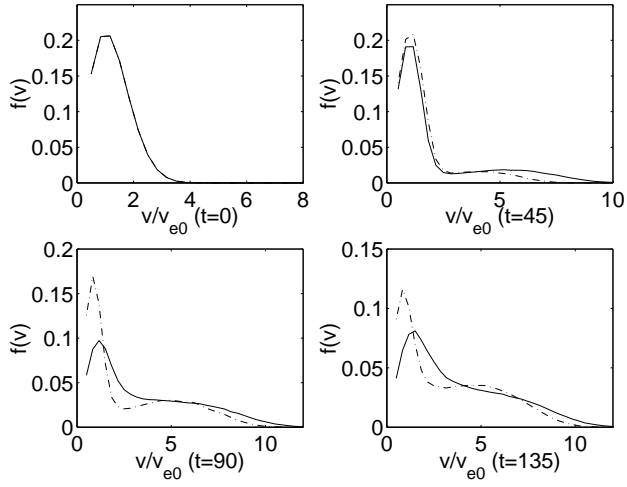


Figure 11: Normalized perpendicular electron speed distributions at various times in the simulations with $u_{b\perp} = 3.25v_{e0}$ (dash-dotted lines) and $u_{b\perp} = 3.5v_{e0}$ (solid lines).

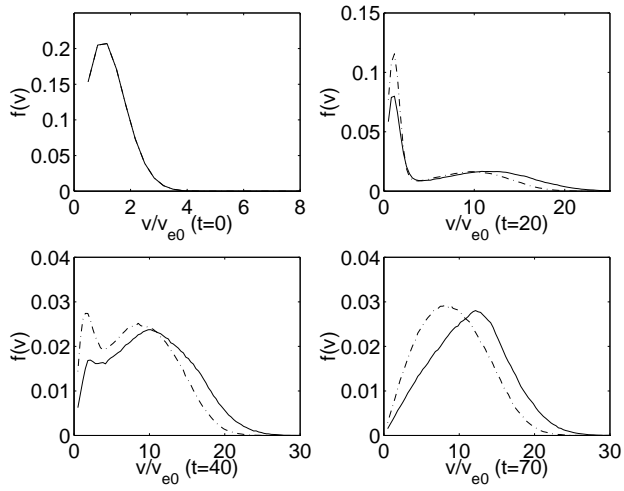


Figure 12: Normalized perpendicular electron speed distributions at various times in the simulations with $u_{b\perp} = 5v_{e0}$ (dash-dotted lines) and $u_{b\perp} = 6v_{e0}$ (solid lines).

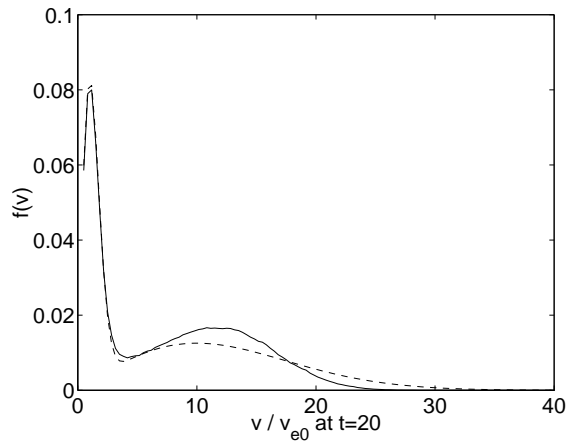


Figure 13: Normalized perpendicular electron speed distribution at $\tilde{t} = 20$ in the simulation with $u_{b\perp} = 6v_{e0}$. The solid curve is the distribution sampled in the simulation; the dashed curve shows a bi-Maxwellian fit.